

# Numerical simulation of atomic layer deposition for thin deposit formation in a mesoporous substrate

Liwei Zhuang<sup>1,2,3</sup>  | Peter Corkery<sup>2,3</sup> | Dennis T. Lee<sup>2,3</sup>  | Seungjoon Lee<sup>2</sup>  |  
Mahdi Kooshkbaghi<sup>4</sup>  | Zhen-liang Xu<sup>1</sup>  | Gance Dai<sup>1</sup> | Ioannis G. Kevrekidis<sup>2</sup> |  
Michael Tsapatsis<sup>2,3,5</sup> 

<sup>1</sup>School of Chemical Engineering, East China University of Science and Technology, Shanghai, China

<sup>2</sup>Department of Chemical and Biomolecular Engineering, Johns Hopkins University, Baltimore, Maryland, USA

<sup>3</sup>Institute for NanoBio Technology, Johns Hopkins University, Baltimore, Maryland, USA

<sup>4</sup>Program in Applied and Computational Mathematics, Princeton University, Princeton, New Jersey, USA

<sup>5</sup>Applied Physics Laboratory, Johns Hopkins University, Laurel, Maryland, USA

## Correspondence

Liwei Zhuang, School of Chemical Engineering, East China University of Science and Technology, 130 Meilong Road, Shanghai 200237, China.

Email: lwzhuang@ecust.edu.cn; lzhuang2@jhu.edu

Michael Tsapatsis, Department of Chemical and Biomolecular Engineering, Johns Hopkins University, 3400 North Charles Street, Baltimore, MD 21218, USA  
Email: tsapatsis@jhu.edu

## Funding information

National Natural Science Foundation of China, Grant/Award Numbers: 21706066, 22078091; China Scholarship Council, Grant/Award Number: 201906745003; U.S. Department of Energy, Office of Science, Office of Basic Energy Sciences, Division of Chemical Sciences, Geosciences and Biosciences under Award, Grant/Award Number: DE-SC0021212

## Abstract

ZnO deposition in porous  $\gamma$ -Al<sub>2</sub>O<sub>3</sub> via atomic layer deposition (ALD) is the critical first step for the fabrication of zeolitic imidazolate framework membranes using the ligand-induced perm-selectivation process (Science, 361 (2018), 1008–1011). A detailed computational fluid dynamics (CFD) model of the ALD reactor is developed using a finite-volume-based code and validated. It accounts for the transport processes within the feeding system and reaction chamber. The simulated precursor spatiotemporal profiles assuming no ALD reaction were used as boundary conditions in modeling diethylzinc reaction/diffusion in porous  $\gamma$ -Al<sub>2</sub>O<sub>3</sub>, the predictions of which agreed with experimental electron microscopy measurements. Further simulations confirmed that the present deposition flux is much less than the upper limit of flux, below which the decoupling of reactor/substrate is an accurate assumption. The modeling approach demonstrated here allows for the design of ALD processes for thin-film membrane formation including the synthesis of metal–organic framework membranes.

## KEYWORDS

atomic layer deposition, computational fluid dynamics, membrane, zeolitic imidazolate framework, zinc oxide

## 1 | INTRODUCTION

Atomic layer deposition (ALD) is a thin-film coating technique enabled by sequential self-terminating reactions between a solid substrate and gaseous reactants. ALD has become a widely used technique in the microelectronics industry<sup>1</sup> and has attracted growing interest from a variety of nanotechnology-based areas.<sup>2,3</sup>

ALD has emerged as a promising technique<sup>4</sup> in preparing membranes and tuning their properties with high precision. ALD-based membrane formation was introduced by Kim and Gavala.<sup>5</sup> They blocked the pores of a Vycor glass tubular substrate with a thin SiO<sub>2</sub> deposit through alternating feeding of gaseous reactants (SiCl<sub>4</sub> and H<sub>2</sub>O) to make H<sub>2</sub> permselective silica membranes. They demonstrated the advantages of ALD compared to the

simultaneous introduction of reactants<sup>6</sup> based on kinetic studies.<sup>7</sup> Other studies have shown that ALD on a membrane's surface or into its pores can adjust the physicochemical properties of the membrane, such as its hydrophilicity<sup>8,9</sup> or its pore size.<sup>10–12</sup> The performance of membranes, such as permeability,<sup>13</sup> selectivity,<sup>14</sup> and antifouling properties,<sup>15</sup> can thus be altered. Additionally, ALD can be used to introduce functional groups into certain porous substrates (e.g., anodic aluminum oxide,  $\alpha$ - $\text{Al}_2\text{O}_3$ , and mesoporous silica) to form hybrid membranes.<sup>16</sup>

ALD reactors and processes for planar wafers have been studied extensively,<sup>17–39</sup> whereas ALD on porous media for membrane preparation has not been investigated at the same level<sup>7,40–49</sup> of detail. A major difference between typical ALD and ALD for thin-film membrane fabrication is that the former aims to completely consume available sites during each ALD cycle. The approach to exhausting all reactive sites, when applied to a porous medium, will result in a thick deposit throughout the medium.<sup>40</sup> The objective of making the deposit as thin as possible requires fast reaction and short reactant pulses to minimize the penetration depth of the deposit inside the support. However, when the reaction is very fast and the pulses are too short, ensuring deposit uniformity across the in-plane directions of the substrate may become a problem due to reactant depletion. Therefore, quantitative models could be useful in guiding ALD process development. Here, the objective of the ALD for the ligand-induced perm-selectivation process<sup>50</sup> is to form ZnO deposit inside the pores of the  $\gamma$ - $\text{Al}_2\text{O}_3$  blocking its pores while minimizing the penetration depth so as to minimize the thickness of the ZIF layer that will be formed when ZnO is exposed to 2-methylimidazole. Deposition on the outside surface of the  $\gamma$ - $\text{Al}_2\text{O}_3$  layer should also be minimized so that formation of a thick ZIF deposit on top of the  $\gamma$ - $\text{Al}_2\text{O}_3$  layer can also be avoided or minimized.

In the present study, a detailed computational model is developed to simulate the transport processes within the ALD reactor

for ZnO deposition. We first focus on the spatiotemporal distributions of precursors within the reactor in the absence of any reaction and use them to establish the boundary conditions for the ALD deposition in the porous support. We then apply these boundary conditions in a model of the reaction/diffusion of diethylzinc (DEZ) in the mesoporous  $\gamma$ - $\text{Al}_2\text{O}_3$  layer. We show that for the specific conditions used in the experiment, the consumption of DEZ by the reaction does not affect its spatiotemporal distribution in the reactor, thus justifying the decoupling of the reactor-scale model from the reaction–diffusion model within the porous substrate. The present study forms the basis of a detailed model on multiscale transport processes coupled with chemical reactions during ultrathin deposit formation in porous substrates for membrane preparation.

## 2 | MODEL AND SIMULATION

The ALD setup (Veeco Savannah S200, Figure 1) mainly consists of the feeding system and reaction chamber with pipeline connections. The feeding system is located in the white box (Figure 1(A)) below the reaction chamber (Figure 1(B)). The temperatures of the feeding system and reaction chamber are controlled through heater jackets and heating inner/outer rings, respectively, using an electronic control box system.

The reactant gases  $\text{Zn}(\text{C}_2\text{H}_5)_2$  (DEZ) and  $\text{H}_2\text{O}$  are supplied in an alternating sequence with an intermediate nitrogen ( $\text{N}_2$ ) purge from the feeding system to the reaction chamber, where a substrate is placed. The inlet (narrow) and outlet (wide) ports are shown in Figure 1(B). The unreacted gases and gaseous side product  $\text{C}_2\text{H}_6$  are purged and captured by a heated trap. In the downstream of the heated trap, a pump is installed to create vacuum throughout the system. A detailed depiction of the entire system is shown in Figure 1(C).

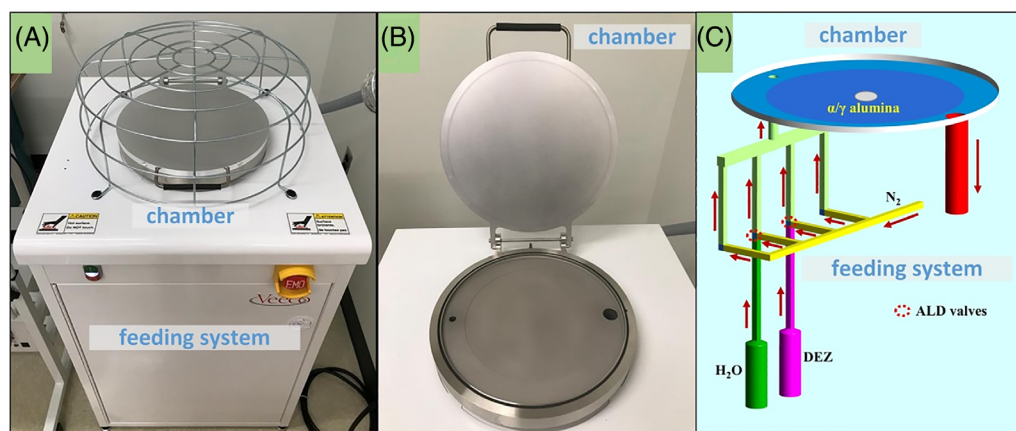


**FIGURE 1** Atomic layer deposition (ALD) setup: (A) entire ALD setup under operation; (B) reaction chamber; (C) detailed arrangement of the ALD reactor indicating feeding system with ALD valves, reaction chamber (diameter of chamber 270 mm) with a substrate (diameter of disc 22 mm) placed in the center. Detailed dimensions are given in Table S1 [Color figure can be viewed at [wileyonlinelibrary.com](http://wileyonlinelibrary.com)]

Two stainless steel containers are nearly half-filled with liquid precursors of DEZ and H<sub>2</sub>O. The remaining space in the container is occupied by the precursor vapor, and the liquid-gas interface is assumed to be in equilibrium. Before the ALD starts, ALD valves for each precursor are closed to avoid the injection of precursor vapor into the reactor caused by the pressure difference across the valve. N<sub>2</sub> carrier gas is continuously supplied into the feeding system and its mass flow rate is regulated with a mass flow controller. When performing ALD, precursors are sequentially pulsed together with a N<sub>2</sub> carrier gas through the corresponding ALD valves. Only the carrier gas flows between each precursor pulse to purge unreacted species and gaseous byproducts from the reaction chamber. The sequence of an ALD ZnO cycle is thus DEZ pulse → N<sub>2</sub> purge → H<sub>2</sub>O pulse → N<sub>2</sub> purge. A piece of α-Al<sub>2</sub>O<sub>3</sub> macroporous disk coated with a ~5-μm γ-Al<sub>2</sub>O<sub>3</sub> mesoporous layer was used as the substrate. The diameter and thickness of the substrate are ~22 and ~2 mm, respectively. During reactant exposures, adsorption/desorption and chemical reactions take place between gaseous reactants and hydroxylated surfaces

inside and outside the porous media.<sup>18,51</sup> The ALD kinetics will be discussed in Section 3.4.

The computational domain regarding the entire reactor was meshed with the software Gambit 2.4.6, and the commercial finite-volume-based code Ansys Fluent 14.5 was used to run the simulation. The meshing information, the governing equations, the boundary and initial conditions, and the simulation algorithm are described in Appendix Sections S1.1 to S1.3. We determined experimentally the consumption of H<sub>2</sub>O during its multiple dosing and purging steps, as well as the pressure profile in the ALD reactor (in the absence of reaction). They were found to be in good agreement with the model predictions (Appendix Section S1.4, Table S3 and Figure S1), providing validation of the model.

### 3 | RESULTS AND DISCUSSION

In this section, the results are organized as follows: visualizing transport processes to present a complete picture of how the reactor is

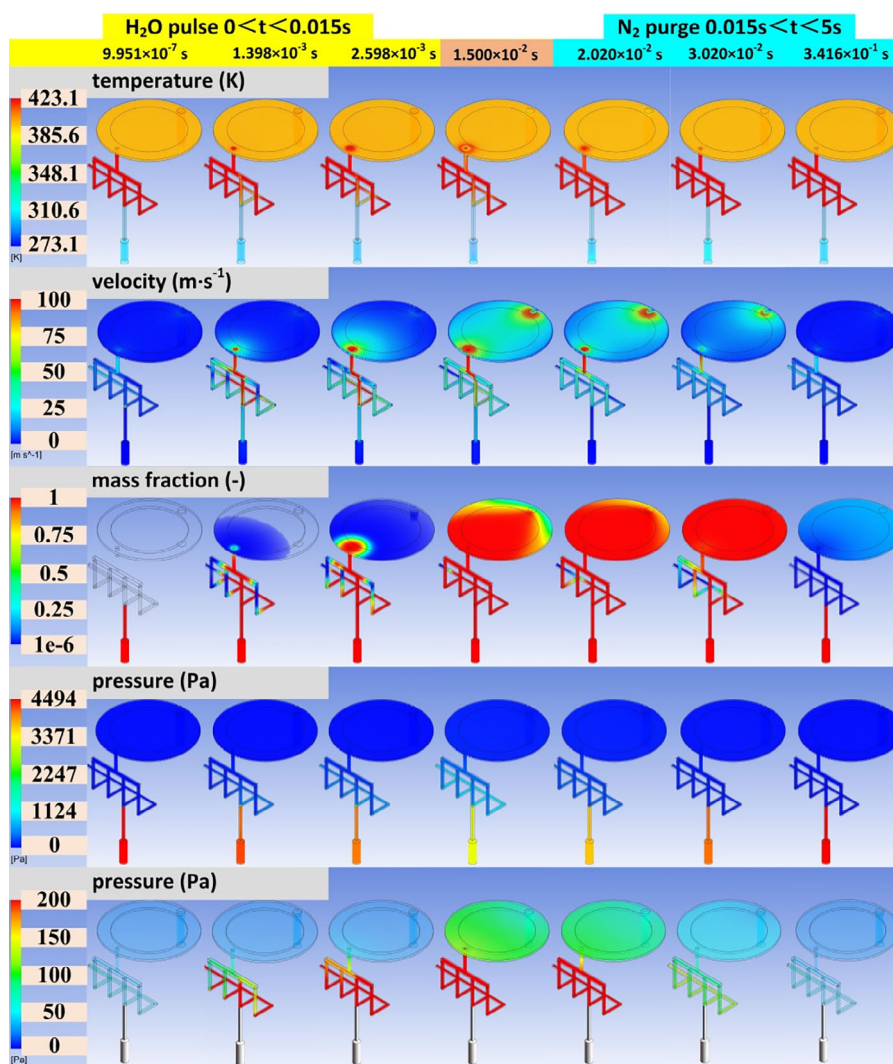


**FIGURE 2** Computational snapshots of the spatiotemporal distributions of temperature, absolute velocity, mass fraction, and pressure within the reactor operated at the standard recipe: (0.015 s H<sub>2</sub>O pulse) → (5 s N<sub>2</sub> purge); the feeding system at 150 °C; the reaction chamber at 125 °C; the H<sub>2</sub>O container at 31 °C. Note that in the last two rows, due to the large difference in pressure inside and outside the container, two different scale bars are chosen (0–4494 and 0–200 Pa) for better visualization of the pressure change [Color figure can be viewed at [wileyonlinelibrary.com](http://wileyonlinelibrary.com)]

operated; presenting spatiotemporal distributions of the precursor partial pressure to quantify the driving force of ALD process in the chamber; plotting the transient precursor partial pressure and total pressure at three typical positions of the substrate to elucidate the process of membrane formation; modeling the reaction/diffusion of DEZ in  $\gamma$ -Al<sub>2</sub>O<sub>3</sub> using the transient profiles as boundary conditions; and modeling the effect of precursor consumption (flux into the porous substrate) on reactor transport processes to determine the strength of the coupling between reactor and substrate scales.

### 3.1 | Visualization of transport processes

In Figure 2, the visualization of transport processes is achieved by presenting the temperature, absolute velocity, mass fraction, and pressure distributions at different times. The half-ALD cycle of H<sub>2</sub>O pulse followed by N<sub>2</sub> purge in the standard recipe is chosen as the example and the container temperature is 31°C. In the present system, the standard recipe is as follows: (0.015 s DEZ pulse) → (5 s N<sub>2</sub> purge) → (0.015 s H<sub>2</sub>O pulse) → (5 s N<sub>2</sub> purge); the feeding system at 150°C (this is the

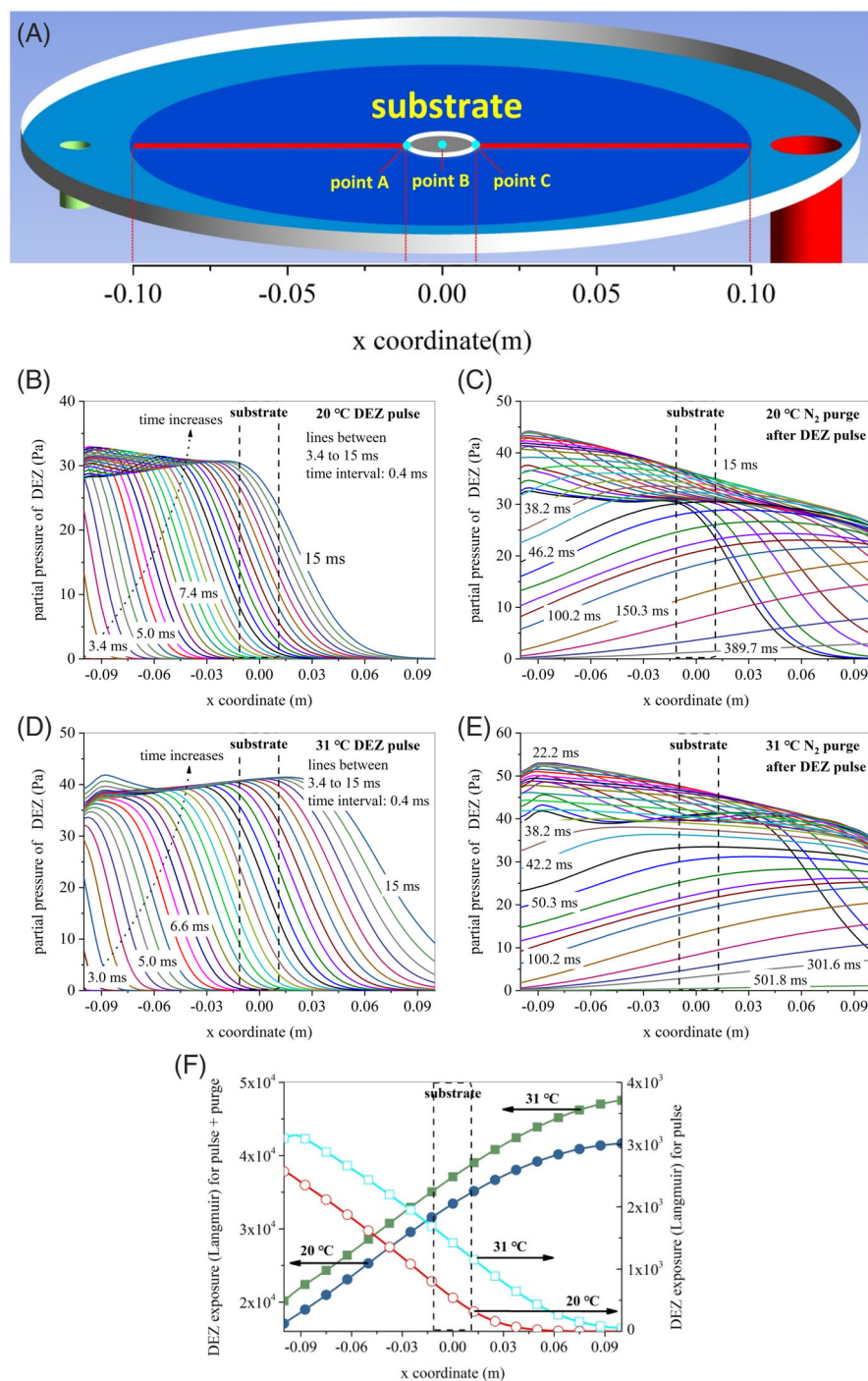


**FIGURE 3** Partial pressure or exposure of diethylzinc (DEZ) in the reaction chamber. (A) geometry and coordinates; (B) DEZ pulse with DEZ container at 20°C; (C) N<sub>2</sub> purge after DEZ pulse in (B); (D) DEZ pulse with DEZ container at 31°C; (E) N<sub>2</sub> purge after DEZ pulse in (D); (F) DEZ exposure for the entire DEZ half-atomic layer deposition (ALD) cycle and the DEZ pulse only (exposure is defined as the product of pressure and time and has the unit of Langmuir or Pa·s, 1 Langmuir =  $1.33 \times 10^{-4}$  Pa·s). The other operating conditions follow the standard ALD recipe: 0.015 s DEZ pulse → 5 s N<sub>2</sub> purge; the feeding system at 150°C; the reaction chamber at 125°C [Color figure can be viewed at [wileyonlinelibrary.com](http://wileyonlinelibrary.com)]

temperature suggested by the reactor manufacturer as extra precaution to avoid any possible condensation of precursors inside the manifold); the reaction chamber at 125°C; and the precursor containers at 31°C.

As shown in Figure 2, the H<sub>2</sub>O vapor is injected into the manifold once the ALD valve is opened. The lower region of the manifold near the ALD valve is cooled down because of the lower temperature of H<sub>2</sub>O vapor, while the H<sub>2</sub>O vapor is heated up after passing the manifold. The inlet region of the reaction chamber is also heated up as a result of the increase in flow rate of heated gas mixture. At 0.015 s, the ALD valve is closed and the temperature distribution returns to its original state within 0.3 s. It is noteworthy that the uniformity of temperature distribution in the reaction chamber is closely related to the flow rate of the upstream gas mixture. Therefore, the size of the substrate susceptor should be properly chosen and the precursor dose should be well controlled. A small-sized substrate, such as the porous membrane with 22 mm diameter used in the present study, should not be greatly affected by the temperature distribution if it is placed at the center of the chamber.

The flow regime in the reactor is laminar, as the Reynolds number is in the range of 0.01 to 10. After the ALD valve is opened, the gas velocity increases to an extremely high value, on the order of 100 m s<sup>-1</sup>, in a very short time span of 1–2 ms. This fast acceleration can be attributed to the large amount of precursor driven by the high pressure difference across the ALD valve. High gas velocity can also be observed near the two ends of the chamber because of the narrow channels of the inlet and outlet.

Initially, the mass fraction of H<sub>2</sub>O is 100% in the H<sub>2</sub>O container and 0% in the rest of the reactor. Once the ALD valve is opened, the H<sub>2</sub>O enters the manifold and mixes with the N<sub>2</sub> carrier gas. The gas mixture expands from the inlet to the entire chamber. The maximum mass fraction of H<sub>2</sub>O can reach approximately 99.9%.

In the last two rows of Figure 2, owing to the large difference in pressure inside and outside the container, two different scale bars are chosen (0 to 4494 Pa and 0 to 200 Pa) for better visualization of the pressure change. The pressure in the precursor container is much higher than in any other region. A decline in pressure in the container takes place after the ALD valve is opened since the H<sub>2</sub>O vapor escapes from the container, indicating that the evaporation at the liquid–gas interface is not fast enough to maintain the pressure. However, the pressure within the container recovers in about 0.34 s following the closure of the ALD valve, which is much shorter than the N<sub>2</sub> purge time of 5 s. This fast recovery of pressure within the precursor containers can guarantee the consistency of precursor dosing in each ALD cycle. As opposed to the pressure change in the container, the pressure in the feeding system and reaction chamber increases once the valve is opened and decreases when the valve is closed. It should be noted that although the maximum pressure in the feeding system can reach 1000 Pa, the scale bar in the last row of Figure 2 is only in the range of 0 to 200 Pa.

Since the precursors are assumed to be ideal gases that behave in an analogous pattern, only the half-ALD cycle of DEZ pulse followed by N<sub>2</sub> purge will be presented in the following sections. The corresponding results for H<sub>2</sub>O are given in Appendix Section S2.

### 3.2 | Spatiotemporal distributions of DEZ partial pressure in the reaction chamber

In this section, the partial pressure of DEZ in the reaction chamber is presented as a function of time, during the half-ALD cycle of DEZ pulse followed by a N<sub>2</sub> purge. The effects of the container temperature are discussed in this section. As one of the most important parameters in ALD, the partial pressure of the precursor has a dominant impact on the rate of precursor diffusion, adsorption/desorption, and chemical reaction within the substrate. As shown in Figure 3(A), the red line connecting the inlet and outlet is chosen as the representative location along which the data regarding DEZ partial pressure versus time are reported. We remind the reader that the substrate in the present study is a disk with the diameter of 22 mm and is placed at the center of the reaction chamber.

As shown in Figure 3(B), after the valve is opened, the leading front of the profile travels toward the substrate gradually. At a time of approximately 7.4 ms, the leading edge of the substrate (marked as point A) experiences the first contact with the DEZ vapor. Afterward, the DEZ partial pressure above the substrate increases with time, whereas the distribution of DEZ partial pressure along the substrate diameter is non-uniform until about 38.2 ms. This spatial distribution of precursor pressure is confirmed by the description from Granneman et al.<sup>52</sup> of cross-flow reactors, in which the trailing edge of the wafer is exposed to more depleted gas than the leading edge. If the substrate had a larger diameter, such as 200 mm, the nonuniformity of DEZ partial pressure distribution could be significant and possibly detrimental to the uniformity of the ALD layer. After the valve is closed, DEZ partial pressure declines with time while the distribution of DEZ partial pressure becomes increasingly more uniform, as shown in Figure 3(C).

As the container temperature increases, the first contact between DEZ and substrate takes place earlier, that is, 6.6 ms for 31°C, as shown in Figure 3(D). The line-average DEZ partial pressure at any moment is higher with a higher container temperature. For example, the line-average DEZ partial pressures at 15 ms are 19.58 and 35.17 Pa for container temperatures of 20 and 31°C, respectively. Additionally, the uniformity of DEZ partial pressure distribution improves with increased container temperatures based on the ratio of the maximum (at  $x = -0.1$  m) to the minimum values (at  $x = 0.1$  m) of DEZ partial pressure at different moments. This is also the case for the H<sub>2</sub>O half-ALD cycle, as shown in Figure S2. Uniform distribution of the precursor vapor pressure<sup>34</sup> is desirable for ALD processes.

In Figure 3(F), DEZ exposure along the red line (Figure 3(A)) is plotted for the entire DEZ half-ALD cycle and the DEZ pulse only (1 Langmuir =  $1.33 \times 10^{-4}$  Pa·s). It shows that at early stage of the DEZ half-ALD cycle (0 to 15 ms), the region near the inlet has higher exposure than the downstream regions. However, for the entire DEZ half-ALD cycle, the total DEZ exposure shows a reverse distribution to the initial one. In general, it is possible that the uniformity of the deposited film will be affected by these nonuniformities. For a large-sized planar substrate, the deposited film thickness may change along the fluid path of the gas mixture.<sup>19,53</sup>

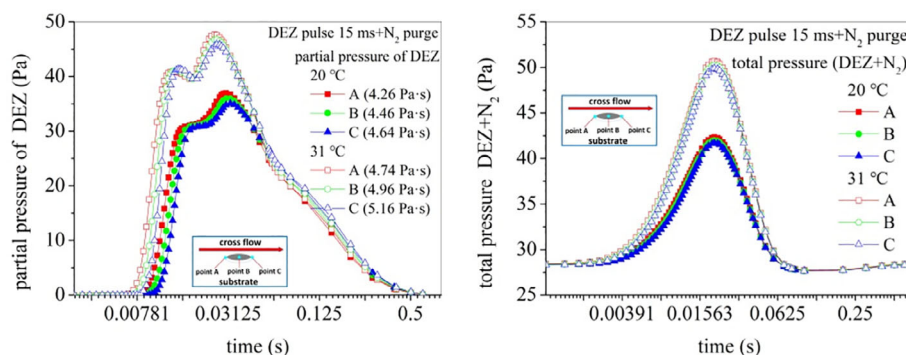


**FIGURE 4** Partial pressure of diethylzinc (DEZ) (A) and total pressure (DEZ + N<sub>2</sub>) (B) at different positions above the substrate with container temperature at 20 and 31°C during DEZ half-atomic layer deposition (ALD) cycle. As shown in the inset schematics, positions A, B, and C correspond to representative upstream, middle, and downstream locations on the substrate. The other operating conditions follow the standard ALD recipe: 0.015 s DEZ pulse → 5 s N<sub>2</sub> purge; the feeding system at 150°C; the reaction chamber at 125°C [Color figure can be viewed at [wileyonlinelibrary.com](http://wileyonlinelibrary.com)]

As will be shown below, for the small substrate we study here, these variations are not significant. However, they must be considered carefully for larger substrates.

### 3.3 | Precursor partial pressure and total pressure above the substrate

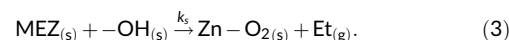
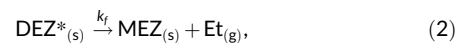
In this section, the transient precursor partial pressure and total pressure (precursor + carrier gas) versus time are presented at three representative locations shown in Figure 3(A): the leading edge nearest to the inlet (point A, upstream); center (point B); and trailing edge nearest to the outlet (point C, downstream) of the substrate.

As shown in Figure 4, owing to the small size of the substrate, the DEZ partial pressures and total pressures are nearly spatially independent. By integrating the DEZ partial pressure over time, we obtain the exposures at three positions above the substrate. In Figure 4(A), the deviations between the maximum and minimum exposures are approximately 8.92% (20°C) and 8.86% (31°C), respectively. This finding indicates that the deposition across the substrate is expected to be uniform; we will discuss this further in the next section. Increasing the container temperature from 20 to 31°C causes an increase in the substrate-average exposure by 11.23%, at the cost of 74.58% extra dosing amount (from Table S3). Similarly, as shown in Figure S3, increasing the dosing amount of H<sub>2</sub>O by 14.5 times (the value is obtained via simulation results) by extending the pulse time from 5 to 100 ms results in only a 2.36 times increase of the substrate-average exposure. It demonstrates that the utilization of precursor will decrease with elevated dosing amount because of the high traveling velocity of precursor at large dosing amount. It also suggests that there should be an optimum range of the dosing that achieves a balance between the precursor consumption and deposition rate.

### 3.4 | Simulation and validation of penetration depth

Previous modeling of the surface reactions in ALD has focused primarily on deposition on planar surfaces or on the thermodynamics of the reactions and thus did not consider mass-transfer limitations and time dependence of the precursor concentration, both of which control the deposition within porous media.<sup>17,39,54–57</sup> This section discusses the development of a model that accounts for the combined reaction and diffusion of DEZ within a mesoporous  $\gamma$ -Al<sub>2</sub>O<sub>3</sub> substrate.

As shown in the set of reactions below (Equations 1–3), the deposition is expected to proceed through a reversible adsorption of DEZ on surface hydroxyls, followed by an irreversible ligand exchange to form monoethylzinc (MEZ) bound to the oxygen of the surface hydroxyl and gaseous ethane (Et<sub>(g)</sub>). MEZ can then further react in a secondary ligand exchange reaction to form a bare Zn atom bridging two underlying oxygen atoms (Zn–O<sub>2(s)</sub>) and an additional ethane molecule.<sup>54</sup>



$k_a$ ,  $k_d$ ,  $k_f$ , and  $k_s$  are the DEZ adsorption, DEZ\* desorption, DEZ\* to MEZ, and MEZ to Zn–O<sub>2</sub> rate constants, respectively. Their values are given in Table S4. Since our objective here is to estimate the maximum penetration depth of Zn species into the substrate, the analysis considered only the first pulse of DEZ. Assuming that the density and reactivity of –OH groups generated during the H<sub>2</sub>O pulse remains the same and that mobility of intermediate species can be neglected, later cycles are not expected to extend the deposition beyond the penetration

depth for the first cycle because of decreased diffusivities caused by pore constriction from the initial ZnO deposit. Moreover, by considering only the first pulse, the added complexity of the effect of pore constriction on DEZ diffusion and changes in the underlying substrate from  $\gamma$ -Al<sub>2</sub>O<sub>3</sub> to ZnO (which affect the reaction rate for subsequent DEZ pulses and the degree of ethyl ligand removal during the H<sub>2</sub>O pulse)<sup>58</sup>

is avoided. In future work, we will attempt to develop a complete model that could account for these phenomena using quartz crystal microbalance data collected for ALD of ZnO on  $\gamma$ -Al<sub>2</sub>O<sub>3</sub> coated substrates.

The differential equations used to model the combined reaction/diffusion problem of the first DEZ pulse are given in Equations (4–7). We neglect the secondary ligand exchange reaction from the above

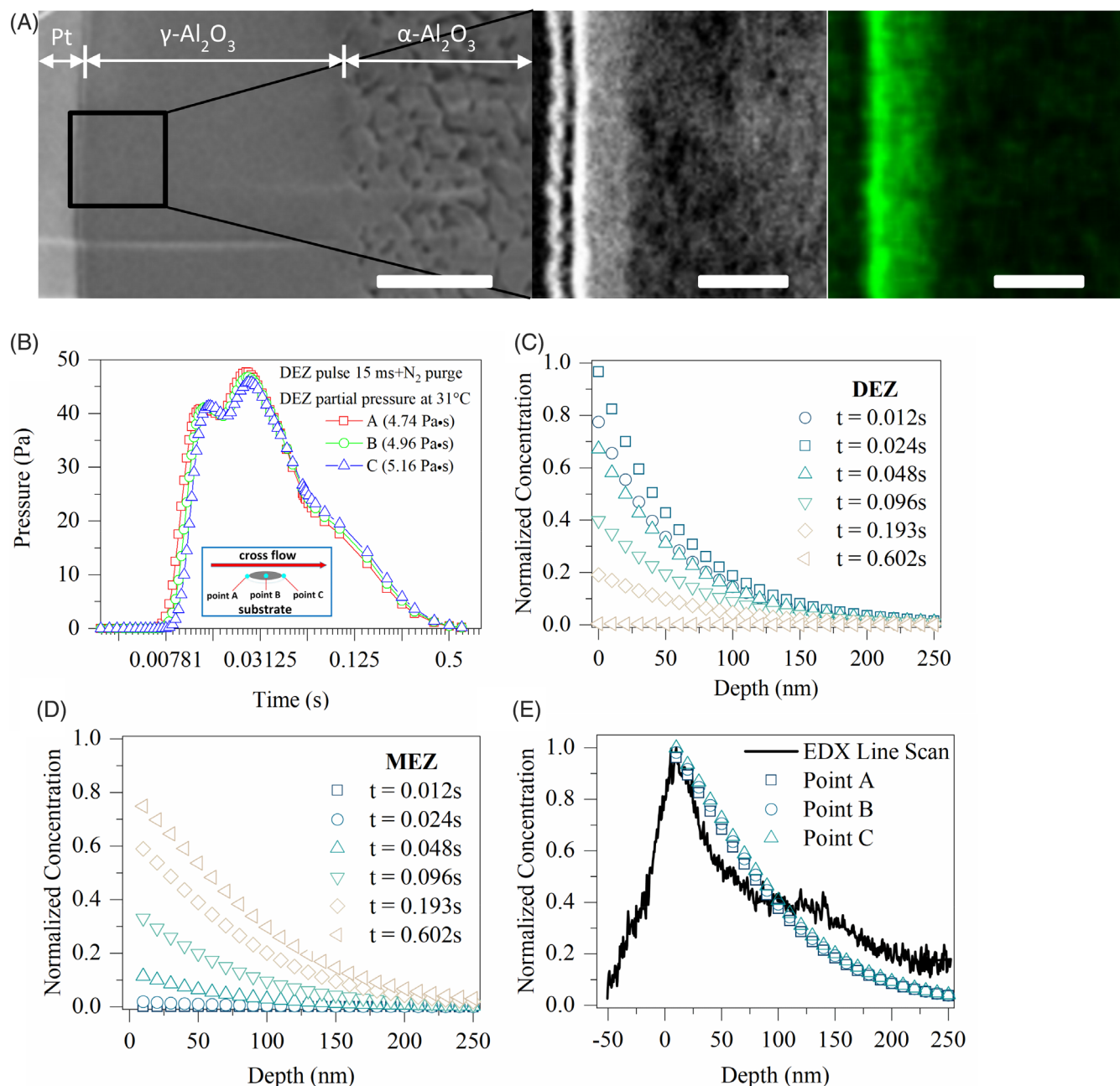


**FIGURE 5** (A) Cross-section of a membrane with ZnO deposit, showing the macroporous  $\alpha$ -Al<sub>2</sub>O<sub>3</sub> and mesoporous  $\gamma$ -Al<sub>2</sub>O<sub>3</sub> support, and higher magnification cross-sectional ADF-STEM and STEM-EDX images of the ZnO deposit (bright contrast and green color) within the  $\gamma$ -Al<sub>2</sub>O<sub>3</sub> layer<sup>50</sup> near the membrane surface (left scale bar: 1  $\mu$ m, middle and right scale bars: 250 nm). (B) Transient diethylzinc (DEZ) boundary conditions determined by the atomic layer deposition reactor model (assuming no reaction) at three positions along the membrane (A, B, and C) as indicated in the inset. (C,D) Concentration profiles of DEZ and MEZ, respectively. (E) Final concentration profile of MEZ at positions A, B, and C compared to profile from cross-sectional TEM imaging.<sup>50</sup> The growth per cycle at the standard recipe on a nonporous substrate is  $\sim$ 0.15 nm. This is not to be confused with the penetration depth when using porous  $\gamma$ -Al<sub>2</sub>O<sub>3</sub>, which under the same conditions is 1000 times larger [Color figure can be viewed at [wileyonlinelibrary.com](http://wileyonlinelibrary.com)]

mechanism because this reaction—although it can affect the DEZ reaction rate (Equation 1) by reducing available —OH species on  $\gamma$ -Al<sub>2</sub>O<sub>3</sub> to react with DEZ—already includes an immobilized MEZ species as a reactant and thus it is not expected to have a dominant effect on the penetration depth of Zn species. The depletion of —OH species by the secondary ligand exchange reaction is also expected to be small during the DEZ pulse due to the high activation energy and, thus, slower reaction rate.<sup>54</sup> The model was developed using centered-finite differences in a MATLAB script.

$$\frac{\partial C_{\text{DEZ}}}{\partial t} = \frac{\partial}{\partial x} \left( \left( \frac{\epsilon}{\tau} \right) D_s \frac{\partial C_{\text{DEZ}}}{\partial x} \right) - k_a C_{\text{DEZ}} C_{\text{OH}} + k_d C_{\text{DEZ}^*}, \quad (4)$$

$$\frac{\partial C_{\text{OH}}}{\partial t} = -k_a C_{\text{DEZ}} C_{\text{OH}} + k_d C_{\text{DEZ}^*}, \quad (5)$$

$$\frac{\partial C_{\text{DEZ}^*}}{\partial t} = k_a C_{\text{DEZ}} C_{\text{OH}} - k_d C_{\text{DEZ}^*} - k_f C_{\text{DEZ}^*}, \quad (6)$$

$$\frac{\partial C_{\text{MEZ}}}{\partial t} = k_f C_{\text{DEZ}^*}. \quad (7)$$

$D_s$  and  $\epsilon/\tau$  are the surface diffusion coefficient and porosity/tortuosity, respectively. Their values are given in Table S4. We use the outcome of the ALD reactor simulation at  $x = 0$  as the time-dependent boundary condition for the concentration of DEZ directly above the membrane surface. This is based on the assumption that the consumption of DEZ by the reaction has negligible effect on the concentration profile within the reactor. This assumption will be validated later in Section 3.5. The boundary condition for DEZ concentration at three different positions on the membrane substrate (i.e., leading (A), center (B), and trailing (C) edge of the substrate disk) as a function of time is shown in Figure 5(B). Although the opening and closing of the valve takes place in 0.015 s, a substantial concentration of DEZ above the support surface persists until ~0.25 s. The differences of the DEZ concentration profiles at positions A, B, and C are very small, with the downstream profiles shifted to longer times, as expected.

The values of the parameters used in the model are shown in Table S4. Reactive hydroxyl concentration was set at 7.8 nm<sup>-2</sup> based on literature values of —OH concentrations on  $\gamma$ -Al<sub>2</sub>O<sub>3</sub> surfaces<sup>59</sup> and considering the differing types of hydroxyls on  $\gamma$ -Al<sub>2</sub>O<sub>3</sub> surfaces.<sup>60,61</sup> DEZ diffusion within the porous  $\gamma$ -Al<sub>2</sub>O<sub>3</sub> substrate was determined to be dominated by surface diffusion rather than Knudsen diffusion, as the majority of the DEZ molecules are expected to be adsorbed on  $\gamma$ -Al<sub>2</sub>O<sub>3</sub> at the temperatures and partial pressures within the ALD reactor.<sup>62</sup> A correlation developed by Sladek et al. was used to calculate the surface diffusivity of DEZ under these conditions.<sup>63</sup> The kinetic parameters  $k_a$ ,  $k_d$ , and  $k_f$  were determined by fitting the penetration depth predicted by the model to the experimental penetration depth determined by energy dispersive X-ray analysis (EDX) as reported in Ref. 50 and shown in Figure 5(A,E). These values are in good agreement with literature values for ALD of ZnO on a ZnO surface<sup>57</sup> (see Appendix Section S5). We note that Figure 5(A,E) is provided here to establish the penetration depth of the ZnO deposit so that it can be compared

with model predictions. Microstructural characteristics of the  $\gamma$ -Al<sub>2</sub>O<sub>3</sub> before and after deposition as well as the structure of the ZnO deposit and its interface with the  $\gamma$ -Al<sub>2</sub>O<sub>3</sub> grains remain unresolved issues due to the small size of the  $\gamma$ -Al<sub>2</sub>O<sub>3</sub> grains (~3 nm) and corresponding pores as well as due to the amorphous nature of the ZnO deposit.

Transient DEZ concentrations at 31°C for the point B in Figure 5(B) were used for the boundary condition at the surface of the substrate in Figure 5(C,D), where concentrations are normalized by the maximum possible value for each species, that is, the initial hydroxyl concentration of 7.8 nm<sup>-2</sup> (or 10,200 mol·m<sup>-3</sup>) for MEZ and maximum DEZ pressure of 47.71 Pa (or 0.01442 mol·m<sup>-3</sup>) shown in Figure 5(B) for DEZ.

The penetration depth of the DEZ—defined here as the depth at which DEZ deposition is 1/10 of that at the substrate surface—was ~200 nm. As shown in Figure 5(E), the concentration profile of MEZ following the first pulse of DEZ predicted by the model is comparable to the EDX line scan obtained from a membrane cross-section.

The process is diffusion-limited since the characteristic time for diffusion of DEZ in the  $L = 5 \mu\text{m}$  thick  $\gamma$ -Al<sub>2</sub>O<sub>3</sub> layer is estimated to be 0.63 ms [ $L^2/(D_s \epsilon/\tau) = (5 \times 10^{-6})^2/(3.96 \times 10^{-7} \times 0.1)$ ], and is much larger than the characteristic time for adsorption (the faster reaction), which is estimated to be  $8.9 \times 10^{-5}$  ms ( $1/(k_a \cdot C_{\text{OH}}) = 1/(1100 \times 10,200)$ ). If the process was not diffusion-limited, then the penetration depth would extend throughout the  $\gamma$ -Al<sub>2</sub>O<sub>3</sub> support because the characteristic time for diffusion (0.63 ms) is smaller than the duration of DEZ half-ALD cycle that exceeds the DEZ pulse (15 ms). The modeled profiles in Figure 5(E) were normalized by the concentration of MEZ at the pore entrance of point C, which is 4% and 2% greater than the corresponding values at points A and B, respectively, and the values from the line scan were normalized by the maximum observed Zn concentration. The non-zero values from the line scan at a depth of less than 0 are due to detection of ZnO on the outside surface of the membrane and therefore are not considered in the comparison with the model.

As shown in Figure S4, there is negligible difference in the penetration depth for Zn species for container temperatures of 20 and 31°C despite the 5% lower concentration of MEZ groups at a container temperature of 20°C relative to 31°C. This lack of sensitivity is important because the container temperatures in the experimental setup are left unregulated at ambient conditions. Experiments indicate that a container left unregulated at room temperature (20°C) will increase in temperature during ALD to 30/31°C as a result of heat transfer from the heated zones of the reactor.

### 3.5 | Coupling between substrate and ALD reactor

Deposition in a porous substrate takes place with boundary conditions set by the reactor-scale transport processes. The transport processes in the reactor can also be influenced by the consumption of reactants as determined by the substrate-scale reaction and diffusion. Therefore, two-way coupling between reactor and substrate processes is possible and its existence should be quantitatively examined in order to determine whether they can be decoupled or not. In the

first three sections of Section 3, simulation results have been given without considering the precursor consumption due to reaction. In Section 3.4, we used the spatiotemporal profiles obtained in the absence of reaction as boundary conditions to determine the penetration depth for the DEZ reaction within the substrate. Here, we perform simulations of cases with fluxes imposed on the substrate surface to see the dependence of coupling intensity on the magnitude of fluxes caused by the reaction/diffusion into the substrate. Only DEZ fluxes are simulated in this section.

We obtained the flux calculated from the reaction/diffusion simulation of Section 3.4, which is the simulation-fitted flux from the model

that fits the experimentally determined penetration depth. By imposing a user-defined function on the substrate surface representing the deposition flux, the simulation is performed allowing coupling between the reactor and substrate. The deposition flux was implemented using a time-dependent boundary condition (updated in each time step) that was imposed on the species transport equation as a DEZ consumption. We first tried a small flux, which is the  $0.57\times$  simulation-fitted flux, and then increased the flux by 5.4, 16.1, 32.3, 53.8, 107.6 times higher than the simulation-fitted flux. The simulation results are given in Figure 6 using the case with no flux as the reference. In Figure 6(A,B), we plot the partial pressure of DEZ versus time at three locations for two cases:

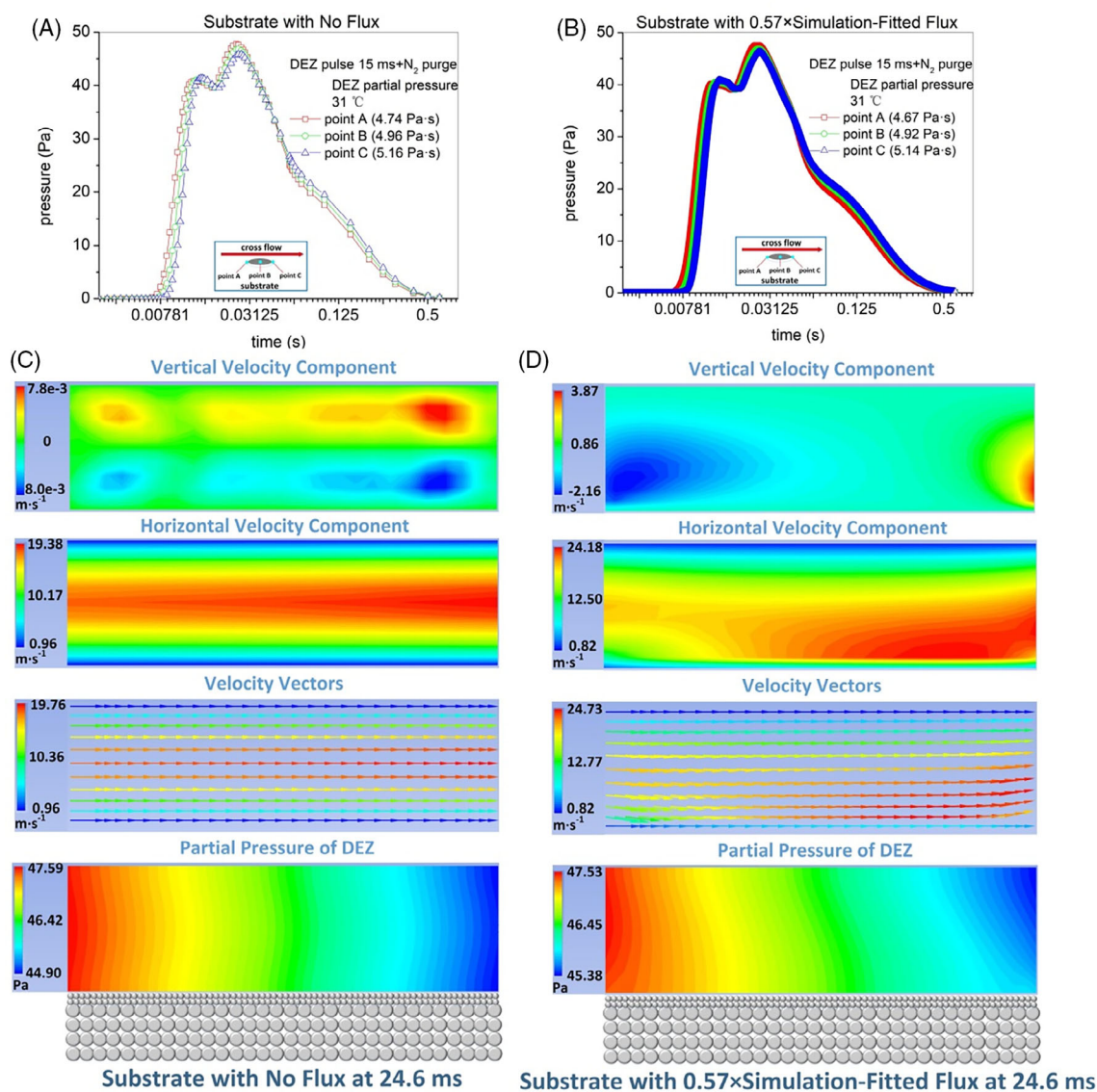


**FIGURE 6** Partial pressures of diethylzinc (DEZ) as a function of time above the substrate with (A) no flux and (B)  $0.57\times$  simulation-fitted flux. Vertical and horizontal velocity components, velocity vectors, and partial pressure of DEZ above the substrate with (C) no flux or (D)  $0.57\times$  simulation-fitted flux. In the simulations shown here, we did not account for the 2 mm thickness of the substrate. The thickness of the substrate is included in Figure S5 and is shown to cause negligible changes on the DEZ profile as a function of time above the substrate [Color figure can be viewed at [wileyonlinelibrary.com](http://wileyonlinelibrary.com)]

no flux and  $0.57\times$  simulation-fitted flux. The exposures are also presented for quantitative comparison. For the  $0.57\times$  simulation-fitted flux, a slight decrease (0.81% to 1.48%) in exposures can be seen, as compared with the case of no flux.

In Figure 6(C,D), the distributions of velocity and partial pressure of DEZ above the substrate are presented with two different surface fluxes (no flux and  $0.57\times$  simulation-fitted flux). The representative instance of  $t = 24.6$  ms is chosen because the partial pressure of DEZ at that moment is near to its maximum value. As shown in Figure 6(C), owing to the absence of deposition, the vertical velocity component is quite low (below  $0.01\text{ m}\cdot\text{s}^{-1}$ ) and the velocity vectors are nearly parallel to the upper surface of the substrate. The partial pressure of DEZ decreases along the substrate and exhibits a symmetric distribution with respect to a horizontal line at the middle height of the chamber. Once a deposition flux in the substrate is imposed, the distributions of velocity and DEZ concentration are altered. As shown in Figure 6(D), a downward vertical velocity component up to  $2.157\text{ m}\cdot\text{s}^{-1}$  can be seen at the leading edge, due to the start of suction, while an upward vertical velocity component up to  $3.869\text{ m}\cdot\text{s}^{-1}$  can be seen at the trailing edge due to the end of suction. This rebound-like velocity profile can be confirmed by the velocity vectors. The region with high velocity migrates to the lower part of chamber and a "boundary layer" with low velocity can be detected near the substrate.

From the description of flow field with the  $0.57\times$  simulation-fitted flux, one can deduce that there will be an upper limit of flux above which the coupling between reactor and substrate can no longer be negligible. Simulations show that the  $16.1\times$  simulation-fitted flux should be approximately regarded as the upper limit of acceptable flux since it shows a negligible disturbance (below 10%, deviation of exposure from the no flux case) to the DEZ exposure. As for the other higher fluxes, the maximum deviations of exposure from the no-flux case can reach 20.16% for  $32.3\times$  simulation-fitted flux and 42.05% for  $107.6\times$  simulation-fitted flux, respectively. At this point we cannot provide suggestions regarding how such high fluxes can be encountered. We only use these high fluxes to indicate the range of validity of the decoupling. One may wonder if the increase in the deposition flux will cause a significant change in the substrate temperature, which will cause disturbance of the DEZ pressure profile above the substrate. To address the role of reaction heat, we have simulated the heat conduction in the direction of substrate thickness, as shown in Appendix Section S6. It shows that for the present case the heat of reaction can be considered to have negligible effect on of the rates of reaction/diffusion within the substrate and DEZ pressure profile above the substrate, even with the DEZ pressure which is 60 times higher than the one in Figure 6(A). However, the effect of temperature change on the transport phenomena/chemical reaction still deserves further investigation if more accurate information is desirable for certain ALD processes.

## 4 | CONCLUSIONS

Transport processes within an ALD reactor were explored via CFD simulation. The dosing amount/rate of precursors were accurately predicted using appropriate models accounting for the precursor

evaporation at the liquid-gas interface and vapor flow through the ALD valve. These integrated models can be applied to the prediction of dosing for a variety of precursors. The dynamic behavior of carrier gas and precursors were presented in the regions of precursor containers and reaction chamber, and can form the basis of further simulation on the interplay between reactor-scale transport processes and substrate-scale deposition.

Simulation of the coupling between the concentration profiles predicted in the absence of the reaction and those obtained by imposing a flux corresponding to reaction and diffusion inside a porous substrate established the upper range of flux below which coupling can be neglected. It was shown that under previously reported conditions typical for ZnO ALD in porous  $\text{Al}_2\text{O}_3$  for membrane formation, the flux of gas reactants in the substrate causes negligible disturbance of the concentration profiles obtained by the ALD reactor model in the absence of reaction. Therefore, the gas pressure profiles can be directly applied as boundary conditions to the reaction-diffusion equations describing deposition inside the porous substrate. The predictions of deposit penetration depth obtained by the reaction-diffusion model agree well with previously reported experimental findings. The model also indicates that for typical laboratory-scale porous substrates (22 mm diameter), deposition takes place uniformly across the substrate, that is, differences in deposition rate and penetration depth between the leading and trailing edges of the substrate can be neglected ensuring a uniform deposit.

The present numerical work can be considered as a first attempt to systematically design ALD-based ultrathin deposit formation in porous substrates for membrane preparation.

## ACKNOWLEDGMENTS

This material is based upon work supported by the U.S. Department of Energy, Office of Science, Office of Basic Energy Sciences, Division of Chemical Sciences, Geosciences and Biosciences under Award DE-SC0021212. LZ acknowledges financial support from the China Scholarship Council (201906745003) and National Natural Science Foundation of China (21706066 and 22078091).

## DATA AVAILABILITY STATEMENT

The data that supports the findings of this study are available in the supplementary material of this article.

## ORCID

Liwei Zhuang  <https://orcid.org/0000-0002-3261-1872>

Dennis T. Lee  <https://orcid.org/0000-0002-1976-2852>

Seungjoon Lee  <https://orcid.org/0000-0003-4586-3574>

Mahdi Kooshkbaghi  <https://orcid.org/0000-0002-6344-7382>

Zhen-liang Xu  <https://orcid.org/0000-0002-1436-4927>

Michael Tsapatsis  <https://orcid.org/0000-0001-5610-3525>

## REFERENCES

1. George SM. Atomic layer deposition: an overview. *Chem Rev.* 2009; 110(1):111-131.
2. Detavernier C, Dendooven J, Sree SP, Ludwig KF, Martens JA. Tailoring nanoporous materials by atomic layer deposition. *Chem Soc Rev.* 2011;40(11):5242-5253.

3. Kim H, Maeng W. Applications of atomic layer deposition to nanofabrication and emerging nanodevices. *Thin Solid Films*. 2009;517(8):2563-2580.
4. Weber M, Julbe A, Ayril A, Miele P, Bechelany M. Atomic layer deposition for membranes: basics, challenges, and opportunities. *Chem Mater*. 2018;30(21):7368-7390.
5. Kim S, Gavalas GR. Preparation of H<sub>2</sub> permselective silica membranes by alternating reactant vapor deposition. *Ind Eng Chem Res*. 1995;34(1):168-176.
6. Tsapatsis M, Kim S, Nam SW, Gavalas GR. Synthesis of hydrogen permselective SiO<sub>2</sub>, TiO<sub>2</sub>, Al<sub>2</sub>O<sub>3</sub>, and B<sub>2</sub>O<sub>3</sub> membranes from the chloride precursors. *Ind Eng Chem Res*. 1991;30(9):2152-2159.
7. Kim S, Gavalas GR. Kinetic study of the reactions of chlorosilanes with porous vycor glass. *J Colloid Interf Sci*. 1993;161(1):6-18.
8. Xu Q, Yang Y, Wang X, et al. Atomic layer deposition of alumina on porous polytetrafluoroethylene membranes for enhanced hydrophilicity and separation performances. *J Membr Sci*. 2012;415-416:435-443.
9. Yang H, Xie Y, Chan H, et al. Crude-oil-repellent membranes by atomic layer deposition: oxide interface engineering. *ACS Nano*. 2018;12(8):8678-8685.
10. Li F, Li L, Liao X, Wang Y. Precise pore size tuning and surface modifications of polymeric membranes using the atomic layer deposition technique. *J Membr Sci*. 2011;385-386:1-9.
11. Shang R, Goulas A, Tang CY, De Frias SX, Rietveld L, Heijman S. Atmospheric pressure atomic layer deposition for tight ceramic nanofiltration membranes: synthesis and application in water purification. *J Membr Sci*. 2017;528:163-170.
12. Jiang Y, Xomeritakis G, Chen Z, et al. Sub-10 nm thick microporous membranes made by plasma-defined atomic layer deposition of a bridged silsesquioxane precursor. *J Am Chem Soc*. 2007;129(50):15446-15447.
13. Wang Q, Wang X, Wang Z, Huang J, Wang Y. PVDF membranes with simultaneously enhanced permeability and selectivity by breaking the tradeoff effect via atomic layer deposition of TiO<sub>2</sub>. *J Membr Sci*. 2013;442:57-64.
14. Xu Q, Yang J, Dai J, Yang Y, Chen X, Wang Y. Hydrophilization of porous polypropylene membranes by atomic layer deposition of TiO<sub>2</sub> for simultaneously improved permeability and selectivity. *J Membr Sci*. 2013;448:215-222.
15. Li N, Tian Y, Zhao J, et al. Static adsorption of protein-polysaccharide hybrids on hydrophilic modified membranes based on atomic layer deposition: anti-fouling performance and mechanism insight. *J Membr Sci*. 2018;548:470-480.
16. Drobek M, Bechelany M, Vallicari C, et al. An innovative approach for the preparation of confined ZIF-8 membranes by conversion of ZnO ALD layers. *J Membr Sci*. 2015;475:39-46.
17. Yanguas-Gil A, Elam JW. Simple model for atomic layer deposition precursor reaction and transport in a viscous-flow tubular reactor. *J Vac Sci Technol A*. 2011;30(1):01A159.
18. Holmqvist A, Magnusson F, Stenström S. Scale-up analysis of continuous cross-flow atomic layer deposition reactor designs. *Chem Eng Sci*. 2014;117:301-317.
19. Holmqvist A, Törndahl T, Stenström S. A model-based methodology for the analysis and design of atomic layer deposition processes—part II: experimental validation and mechanistic analysis. *Chem Eng Sci*. 2013;94:316-329.
20. Holmqvist A, Törndahl T, Stenström S. A model-based methodology for the analysis and design of atomic layer deposition processes—part III: constrained multi-objective optimization. *Chem Eng Sci*. 2013;96:71-86.
21. Holmqvist A, Törndahl T, Stenström S. A model-based methodology for the analysis and design of atomic layer deposition processes—part I: mechanistic modelling of continuous flow reactors. *Chem Eng Sci*. 2012;81:260-272.
22. Shaeri MR, Jen T, Yuan CY, Behnia M. Investigating atomic layer deposition characteristics in multi-outlet viscous flow reactors through reactor scale simulations. *Int J Heat Mass Transf*. 2015;89:468-481.
23. Shaeri MR, Jen T, Yuan CY. Reactor scale simulation of an atomic layer deposition process. *Chem Eng Res Design*. 2015;94:584-593.
24. Shaeri MR, Jen T, Yuan CY. Improving atomic layer deposition process through reactor scale simulation. *Int J Heat Mass Transf*. 2014;78:1243-1253.
25. Pan D. Numerical study on the effectiveness of precursor isolation using N<sub>2</sub> as gas barrier in spatial atomic layer deposition. *Int J Heat Mass Transf*. 2019;144:118642.
26. Pan D, Jen T, Yuan C. Effects of gap size, temperature and pumping pressure on the fluid dynamics and chemical kinetics of in-line spatial atomic layer deposition of Al<sub>2</sub>O<sub>3</sub>. *Int J Heat Mass Transf*. 2016;96:189-198.
27. Pan D, Ma L, Xie Y, Jen TC, Yuan C. On the physical and chemical details of alumina atomic layer deposition: a combined experimental and numerical approach. *J Vac Sci Technol A*. 2015;33(2):021511.
28. Pan D, Ma L, Xie Y, Wang F, Jen T, Yuan C. Experimental and numerical investigations into the transient multi-wafer batch atomic layer deposition process with vertical and horizontal wafer arrangements. *Int J Heat Mass Transf*. 2015;91:416-427.
29. Pan D, Li T, Chien Jen T, Yuan C. Numerical modeling of carrier gas flow in atomic layer deposition vacuum reactor: a comparative study of lattice Boltzmann models. *J Vac Sci Technol A*. 2013;32(1):01A110.
30. Xie Y, Pan D, Ma L, Yuan C. Optimizing the process efficiency of atomic layer deposition of alumina for its sustainability improvement: a combined experimental and modeling study. *J Clean Prod*. 2016;133:338-347.
31. Xie Y, Ma L, Pan D, Yuan C. Mechanistic modeling of atomic layer deposition of alumina process with detailed surface chemical kinetics. *Chem Eng J*. 2015;259:213-220.
32. Gakis GP, Vergnes H, Scheid E, Vahlas C, Boudouvis A, Caussat B. Detailed investigation of the surface mechanisms and their interplay with transport phenomena in alumina atomic layer deposition from TMA and water. *Chem Eng Sci*. 2019;195:399-412.
33. Peltonen P, Vuorinen V, Marin G, Karttunen AJ, Karppinen M. Numerical study on the fluid dynamical aspects of atomic layer deposition process. *J Vac Sci Technol A*. 2018;36(2):021516.
34. Gakis GP, Vergnes H, Scheid E, Vahlas C, Caussat B, Boudouvis A. Computational fluid dynamics simulation of the ALD of alumina from TMA and H<sub>2</sub>O in a commercial reactor. *Chem Eng Res Design*. 2018;132:795-811.
35. Zhang Y, Ding Y, Christofides PD. Multiscale computational fluid dynamics modeling of thermal atomic layer deposition with application to chamber design. *Chem Eng Res Design*. 2019;147:529-544.
36. Ding Y, Zhang Y, Ren YM, Orkoulas G, Christofides PD. Machine learning-based modeling and operation for ALD of SiO<sub>2</sub> thin-films using data from a multiscale CFD simulation. *Chem Eng Res Design*. 2019;151:131-145.
37. Ding Y, Zhang Y, Kim K, Tran A, Wu Z, Christofides P. Microscopic modeling and optimal operation of thermal atomic layer deposition. *Chem Eng Res Design*. 2019;145:159-172.
38. Van Bui H, Grillo F, Van Ommen JR. Atomic and molecular layer deposition: off the beaten track. *Chem Commun*. 2017;53(1):45-71.
39. Cremers V, Puurunen RL, Dendooven J. Conformality in atomic layer deposition: current status overview of analysis and modelling. *Appl Phys Rev*. 2019;6(2):021302.
40. Elam JW, Routkevitch D, Mardilovich PP, George SM. Conformal coating on ultrahigh-aspect-ratio Nanopores of anodic alumina by atomic layer deposition. *Chem Mater*. 2003;15(18):3507-3517.
41. Fang W, Tang Y, Ban C, Kang Q, Qiao R, Tao W. Atomic layer deposition in porous electrodes: a pore-scale modeling study. *Chem Eng J*. 2019;378:122099.

42. Ylilampi M, Ylivaara OM, Puurunen RL. Modeling growth kinetics of thin films made by atomic layer deposition in lateral high-aspect-ratio structures. *J Appl Phys*. 2018;123(20):205301.
43. Keuter T, Menzler NH, Mauer G, Vondahlen F, Vaßen R, Buchkremer H. Modeling precursor diffusion and reaction of atomic layer deposition in porous structures. *J Vac Sci Technol A*. 2014;33(1):01A104.
44. Yanguas-Gil A, Elam JW. A Markov chain approach to simulate atomic layer deposition chemistry and transport inside nanostructured substrates. *Theor Chem Acc*. 2014;133(4):1465.
45. Adomaitis RA. A ballistic transport and surface reaction model for simulating atomic layer deposition processes in high-aspect-ratio Nanopores. *Chem Vapor Depos*. 2011;17(10–12):353-365.
46. Dwivedi V, Adomaitis RA. Multiscale simulation and optimization of an atomic layer deposition process in a nanoporous material. *ECS Trans*. 2009;25(8):115.
47. Gordon RG, Hausmann D, Kim E, Shepard J. A kinetic model for step coverage by atomic layer deposition in narrow holes or trenches. *Chem Vapor Depos*. 2003;9(2):73-78.
48. Gobbert MK, Prasad V, Cale TS. Modeling and simulation of atomic layer deposition at the feature scale. *J Vac Sci Technol B*. 2002;20(3):1031-1043.
49. Gobbert MK, Prasad V, Cale TS. Predictive modeling of atomic layer deposition on the feature scale. *Thin Solid Films*. 2002;410(1):129-141.
50. Ma X, Kumar P, Mittal N, et al. Zeolitic imidazolate framework membranes made by ligand-induced permselectivation. *Science*. 2018;361(6406):1008-1011.
51. Holmqvist A, Törndahl T, Magnusson F, Zimmermann U, Stenström S. Dynamic parameter estimation of atomic layer deposition kinetics applied to in situ quartz crystal microbalance diagnostics. *Chem Eng Sci*. 2014;111:15-33.
52. Granneman E, Fischer P, Pierreux D, Terhorst H, Zagwijn P. Batch ALD: characteristics, comparison with single wafer ALD, and examples. *Surf Coat Tech*. 2007;201(22):8899-8907.
53. Henn-Lecordier L, Anderle M, Robertson E, Rubloff GW. Impact of parasitic reactions on wafer-scale uniformity in water-based and ozone-based atomic layer deposition. *J Vac Sci Technol A*. 2011;29(5):051509.
54. Weckman T, Laasonen K. Atomic layer deposition of zinc oxide: diethyl zinc reactions and surface saturation from first-principles. *J Phys Chem C*. 2016;120(38):21460-21471.
55. Weckman T, Shirazi M, Elliott SD, Laasonen K. Kinetic Monte Carlo study of the atomic layer deposition of zinc oxide. *J Phys Chem C*. 2018;122(47):27044-27058.
56. Weckman T, Laasonen K. Atomic layer deposition of zinc oxide: study on the water pulse reactions from first-principles. *J Phys Chem C*. 2018;122(14):7685-7694.
57. Kim S, Lee S, Ham S, et al. A kinetic study of ZnO atomic layer deposition: effects of surface hydroxyl concentration and steric hindrance. *Appl Surf Sci*. 2019;469:804-810.
58. Mackus AJ, Maclsaac C, Kim W, Bent SF. Incomplete elimination of precursor ligands during atomic layer deposition of zinc-oxide, tin-oxide, and zinc-tin-oxide. *J Chem Phys*. 2017;146(5):052802.
59. Knözinger H, Ratnasamy P. Catalytic aluminas: surface models and characterization of surface sites. *Catal Rev*. 1978;17(1):31-70.
60. Shirai T, Watanabe H, Fuji M, Takahashi M. Structural properties and surface characteristics on aluminum oxide powders. *Ceram Res Lab*. 2009;9:23-31.
61. Wefers K, Misra C. *Oxides and Hydroxides of Aluminum*. Pittsburgh, PA: Alcoa Laboratories; 1987.
62. Baumgarten E, Weinstrauch F, Höffkes H. Adsorption isotherms of hydrocarbons on  $\gamma$ -alumina. *J Chromatogr A*. 1977;138(2):347-354.
63. Sladek KJ, Gilliland ER, Baddour RF. Diffusion on surfaces. II. Correlation of diffusivities of physically and chemically adsorbed species. *Ind Eng Chem Res Fund*. 1974;13(2):100-105.

#### SUPPORTING INFORMATION

Additional supporting information may be found online in the Supporting Information section at the end of this article.

**How to cite this article:** Zhuang L, Corkery P, Lee DT, et al. Numerical simulation of atomic layer deposition for thin deposit formation in a mesoporous substrate. *AIChE J*. 2021; e17305. <https://doi.org/10.1002/aic.17305>